A Fast Electro-Thermal Model of Traction Inverters for Electrified Vehicles

Jin Ye, *Member, IEEE*, Kai Yang, Haizhong Ye, and Ali Emadi, *Fellow, IEEE*

***Abstract*—In this paper, a fast electro-thermal model of traction inverters for electrified vehicles is proposed. First, a thermal model considering the thermal coupling is presented and experimentally verified. The impact of the thermal spreading effect, heat convection, and temperature-dependent material thermal properties on the accuracy of the linear assumption is investigated by ANSYS-Fluent simulation. In order to reduce the influence of the temperature-dependent thermal conductivity on the accuracy of the thermal model, the average temperature is applied to determine the thermal conductivity of the power module package. Second, an accurate temperature-dependent switching power loss model is represented as the lookup table through experimental measurements. In order to simplify the lookup table, the switching power loss is considered proportional to the dc-link voltage and, therefore, the inputs of the lookup table are current and temperature. Finally, a scheme to speed up the online junction temperature estimation is proposed by considering both the thermal network properties and the required accuracy. With the proposed calculation rate determination method, the total computational time for the junction temperature estimation is reduced significantly.**

***Index Terms*—Electric and hybrid electric vehicles, electro-thermal model, inverters, nonlinear effect, temperature-dependent loss model, thermal coupling, traction systems.**

I. INTRODUCTION

POWER converters with very high reliability are required for electrified vehicles. The thermal stress introduced by the massive time-varying loss-of-power semiconductor devices reduces the lifetime of the power modules [1]–[6]. Several failure modes due to the thermo-mechanical breakdown of power modules are presented in [7]–[9], and the power module lifetime is mainly determined by the average and fluctuation of the junction temperatures [10]–[12]. Besides, the online overtemperature protection of power modules is essential to improve the reliability of traction inverters. Since the electrical characteristics of power devices are temperature dependent, a fast and accurate electro-thermal model is required to get the actual power losses and junction temperatures.

An electro-thermal model includes the thermal model and the temperature-dependent power loss model. The thermal modeling methods include numerical approach, analytical approach, and thermal resistor–capacitor (*RC*) network. The numerical approach, including the finite element method [13] and computational fluid dynamics (CFD) [14], can provide accurate temperature distribution with any device geometry. However, it is very time-consuming and, therefore, it is not applicable for evaluating the junction temperature for long-time load profiles [15]. The analytical approach provides a Fourier series solution by solving the one-dimensional, second-dimensional, and three-dimensional (3-D) heat diffusion equations [16]–[18]. This “mesh-less” method offers an improved tradeoff between the accuracy and computing speed. But they can only be used to describe the heat conduction in the power module packages with simple structures. The heat convection between the heat sink and the coolant cannot be accurately evaluated. The thermal *RC* network is a computationally efficient thermal model that can be easily integrated into circuit simulators [19]–[22]. However, this approach focuses mainly on the modeling of the power modules. The application of the *RC* network to the entire system has not been validated. Also, the prerequisite of the thermal network is that the system is a linear time-invariant (LTI) system. Therefore, the accuracy of the linear assumption needs to be evaluated. A method is proposed to consider the temperature-dependent material properties by using the temperature-dependent thermal network parameters [23]. The parameters have to be tuned according to the temperature, which increases the complexity.

The temperature-dependent power loss model is the other part of the electro-thermal model. There are different approaches to get the power loss: the physical-based model [24] and the experimental measurement [25]. The switching losses of power devices are sensitive to the driver circuit and the stray inductance. Therefore, it is better to get the accurate switching losses through experimental measurement. Besides, for the long-time online and offline junction temperature estimation, the computational speed is vital. In [26], a high-speed electro-thermal model is proposed by averaging the power loss for every several switching cycles. With this model, the junction temperature is not required for each switching cycle; however, the power loss is calculated at each switching cycle in order to get the average power loss for every several switching cycles. This will also partly reduce the speed of the electro-thermal model, which may not be a viable solution to online junction temperature estimation.

Manuscript received December 24, 2015; revised May 12, 2016 and March 12, 2016; accepted June 17, 2016. Date of publication June 28, 2016; date of current version February 2, 2017. Recommended for publication by Associate Editor T. M. Lebey.

J. Ye is with the Department of Electrical Engineering, San Francisco State University, San Francisco, CA 94132 USA (e-mail: jinye@sfsu.edu).

K. Yang is with the Bombardier Transportation, Inc., Kingston, ON K7K 2H6 Canada (e-mail: kyflying@hotmail.com).

H. Ye is with the Schneider Electric, Burnaby, BC V5G 4M1 Canada (e-mail: haizhong.ye.xjtu@gmail.com).

A. Emadi is with the McMaster Institute for Automotive Research and Technology, McMaster University, Hamilton, ON L8P OA6 Canada (e-mail: emadi@mcmaster.ca).

Color versions of one or more of the figures in this paper are available online at http://ieeexplore.ieee.org.

Digital Object Identifier 10.1109/TPEL.2016.2585526

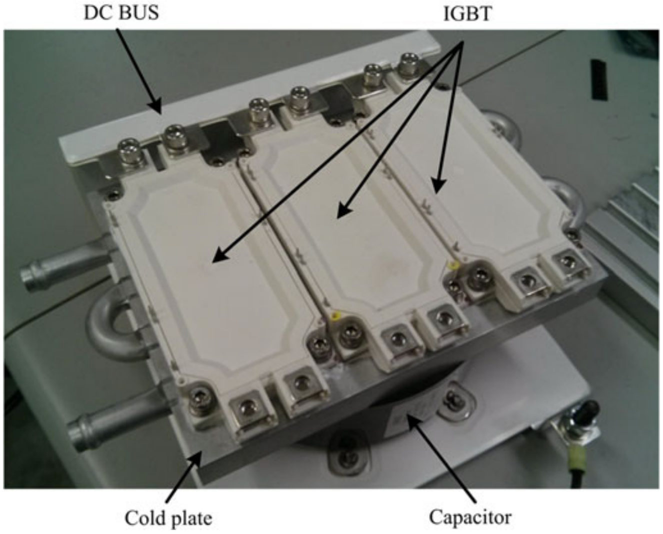

Fig. 1. System configuration of the traction inverter.

This paper presents an accurate and fast electro-thermal model for the entire traction inverter used in electrified vehicles. The main contributions of this paper include

1) The impact of the thermal spreading effect, heat convection, and temperature-dependent material thermal properties on the accuracy of the linear assumption is comprehensively investigated by the ANSYS-Fluent simulation. Compared to the temperature-dependent thermal conductivity, the thermal coupling and the thermal spreading effect have a negligible impact on the linear assumption.
2) In order to reduce the influence of the temperature-dependent thermal conductivity on the accuracy of the thermal model, the average temperature is applied to determine the thermal conductivity of the material in the power module.
3) The switching power loss under different temperatures and currents are measured by the double-pulse test. The switching loss is considered proportional to the dc-link voltage and the switching losses are stored as a lookup table with inputs: the junction temperature and currents.
4) A high-speed model is proposed, which considers both the thermal network properties and the required accuracy of the temperature estimation. With the proposed method to determine the calculation rate of junction temperature, the speed can be improved significantly.

II. THERMAL MODEL CONSIDERING THE THERMAL COUPLING

A. System Configuration

A traction inverter is applied to the electro-thermal modeling, as shown in Fig. 1. It consists of a liquid-cooled cold plate, a dc bus, a capacitance, and three insulated-gate bipolar transistor (IGBT) modules. Only power modules and cold plate are considered for the thermal modeling. The detailed 3-D model of the power module is shown in Fig. 2(a). The power module consists of six IGBTs and six diodes. Three IGBTs or diode chips are connected in parallel and, therefore, they can be classified as four devices: high-side IGBT #1, low-side IGBT #2, high-side diode #3, and low-side diode #4. The vertical structure of material layers is illustrated in Fig. 2(b).

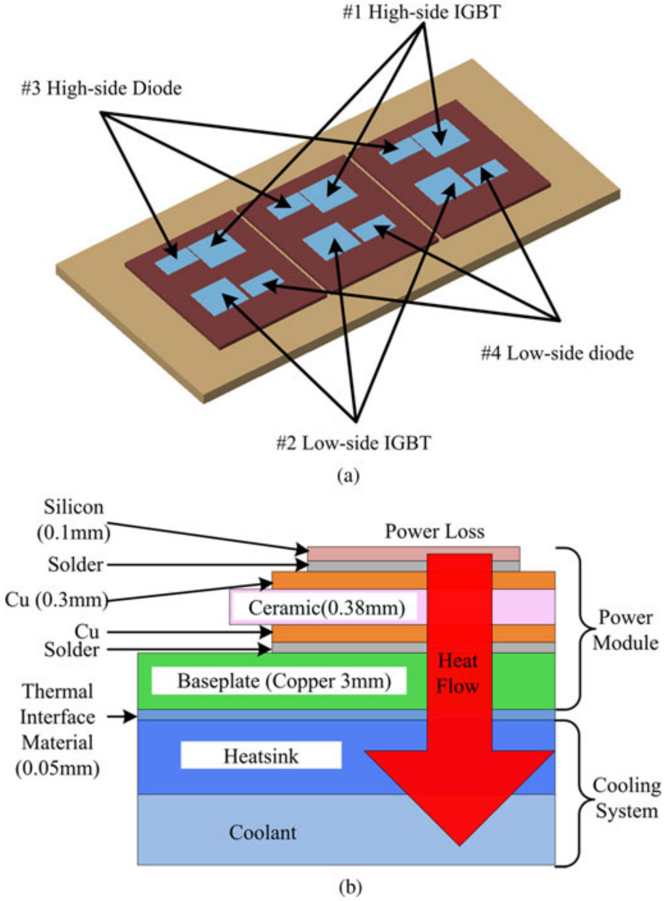

Fig. 2. Internal architecture of the power module: (a) detailed 3-D model, (b) the vertical structure.

B. Thermal Model Considering the Thermal Coupling

Several parameters are defined as follows to derive the thermal model.

$P_j(t)$ $(j = 1, 2, 3, 4)$ The instantaneous power dissipation at device #*j*.

$Z_{\mathrm{ij\_}s}(t)$ $(i, j = 1, 2, 3, 4)$ The transient thermal impedance (from the junction to coolant) of device #*i* by adding the step power dissipation at device #*j*.

$Z_{\mathrm{ij}}(t)$ $(i, j = 1, 2, 3, 4)$ The transient thermal impedance (from the junction to coolant) of device #*i* by adding the impulse power dissipation at #*j*.

$T_i(t)$ $(i = 1, 2, 3, 4)$ The instantaneous junction temperature of device #*i*.

$T_c(t)$ The coolant temperature.

The transient thermal impedance $Z_{\mathrm{ij\_}s}(\mathrm{t})$ with the step power dissipation at device #*j* is defined as

$$Z_{\mathrm{ij\_}s}(t) = \frac{T_i(t) - T_c(t)}{P_j(t)}. \quad (1)$$

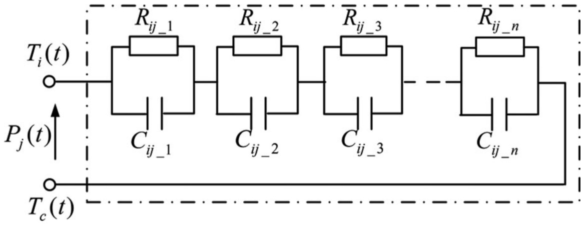

Fig. 3. Structure of the Foster network.

The transient thermal impedance $Z_{\mathrm{ij}}(\mathrm{t})$ with the impulse power dissipation is derived as

$$Z_{\mathrm{ij}}(t) = \frac{dZ_{\mathrm{ij}\_s}(t)}{dt}. \tag{2}$$

If the LTI assumption of the thermal transfer process is made, the junction temperatures with arbitrary power losses are represented by the matrix-vector form in *s* domain, shown as

$$\begin{bmatrix} T_1(s) \\ T_2(s) \\ T_3(s) \\ T_4(s) \end{bmatrix} = \begin{bmatrix} Z_{11}(s) & Z_{12}(s) & Z_{13}(s) & Z_{14}(s) \\ Z_{21}(s) & Z_{22}(s) & Z_{23}(s) & Z_{24}(s) \\ Z_{31}(s) & Z_{32}(s) & Z_{33}(s) & Z_{34}(s) \\ Z_{41}(s) & Z_{42}(s) & Z_{43}(s) & Z_{44}(s) \end{bmatrix} \begin{bmatrix} P_1(s) \\ P_2(s) \\ P_3(s) \\ P_4(s) \end{bmatrix} + T_c(s) \tag{3}$$

where $Z_{\mathrm{ij}}(\mathrm{s})$ is the Laplace transform of the impulse response $Z_{\mathrm{ij}}(\mathrm{t})$. When $i = j$, the elements of the impedance matrix represent the self-heating effects. The other elements represent the cross-heating effects between different devices.

In order to get the junction temperatures, the thermal impedance matrix needs to be obtained. The Foster network, as shown in Fig. 3, has the similar dynamic response as that of the heat transfer in power converters. Therefore, the circuit impedance of it can represent the thermal impedance elements in (3). The transfer function of the Foster network is derived as

$$Z_{\mathrm{ij}}(s) = \sum_{m=1}^{n} \frac{R_{\mathrm{ij}\_m}/\tau_{\mathrm{ij}\_m}}{s + 1/\tau_{\mathrm{ij}\_m}} \tag{4}$$

where *n* indicates the number of order of the Foster network; the thermal time constant $\tau_{\mathrm{ij}\_m} = R_{\mathrm{ij}\_m} \times C_{\mathrm{ij}\_m}$..

Equation (4) can be converted to the *z*-domain transfer function (5) by using the zero-hold transform method, where T_s is the sampling period. If the parameters R_{ij_m} and τ_{ij_m} are obtained, the junction temperatures of devices can be calculated with microcontrollers by using the z-domain form of (3)

$$\begin{aligned} Z_{\mathrm{ij}}(z) &= \sum_{m=1}^{n} \frac{b_{\mathrm{ij}\_m} z^{-1}}{1 + a_{\mathrm{ij}\_m} z^{-1}} R_{\mathrm{ij}\_m};\ b_{\mathrm{ij}\_m} = \frac{T_s}{\tau_{\mathrm{ij}\_m}}, \\ a_{\mathrm{ij}\_m} &= b_{\mathrm{ij}\_m} - 1. \end{aligned} \tag{5}$$

The step response of the Foster network is represented as a series consisting of a finite number of exponential terms as given in

$$Z_{\mathrm{ij}\_s}(t) = \sum_{m=1}^{n} R_{\mathrm{ij}\_m}\left(1 - exp\left(-\frac{t}{\tau_{\mathrm{ij}\_m}}\right)\right). \tag{6}$$

In order to get the parameters of the Foster network, the step response thermal impedances need to be obtained first. Then, with the curve fitting of the obtained step responses in the form of (6), the parameters R_{ij_m} and τ_{ij_m} can be obtained.

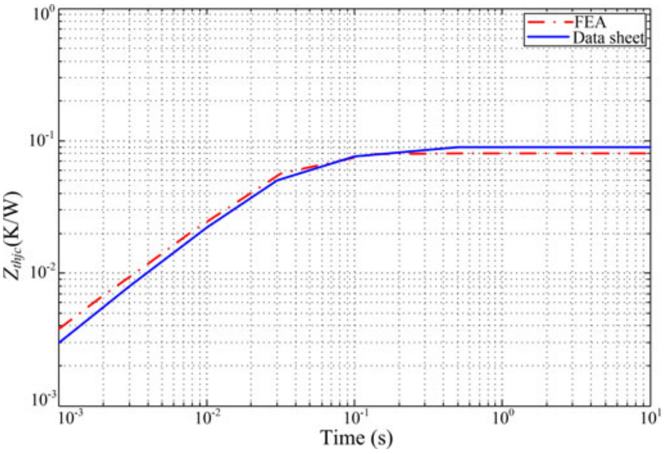

Fig. 4. Comparison of the step response transient thermal impedance.

TABLE I
BOUNDARY CONDITIONS OF THE TRANSIENT THERMAL MODEL IN FLUENT

Coolant temperature at inlet	338.15 K (65 °C)
Working fluid	50% ethylene glycol 50% water mixture
Flow rate	2 L/min
Power dissipation	100 W per chip (300 W per device)
Maximum allowable pressure drop	5 lbf/in^2
Ambient temperature	333.15 K (60 °C) in the case, 308.15 K (35 °C) in the ambient
Coefficient of convection with air	6 W/m^2 K^{-1} in the case, 12 W/m^2 K^{-1} in the cabinet
Thickness of the thermal interface material layer	0.05 mm

In this paper, the transient thermal analysis with the ANSYS-Fluent tool is applied to get the step responses. In order to verify the accuracy of the transient thermal simulation, the step response transient thermal impedance curve obtained by Finite element analysis (FEA) simulation is compared to that in the datasheet, which is obtained by using the temperature-sensitive electrical parameters (TSEPs) measurement method. In order to make a fair comparison, the simulation boundary conditions are the same as the measurement conditions of the thermal curve in the datasheet. The comparison of the FEA simulation result and the transient thermal impedance curve provided in the datasheet is shown in Fig. 4. Z_{thjc} is the thermal impedance from the IGBT junction to the case. It can be found that these two curves are very close to each other in the whole time range. The steady-state value of the thermal impedance obtained from FEA is a little smaller than that in the datasheet, and the error is within 5%. Therefore, the accuracy of the FEA simulation is validated, which is applied to the transient thermal analysis.

The boundary conditions for the thermal simulation are listed in Table I. The junction temperature profiles of all devices are recorded by adding the constant power dissipation at each device one by one. The average temperature of the top surfaces of the device is regarded as its junction temperature [27]. With the junction temperature profiles and the definition of (1), the step response thermal impedances can be derived.

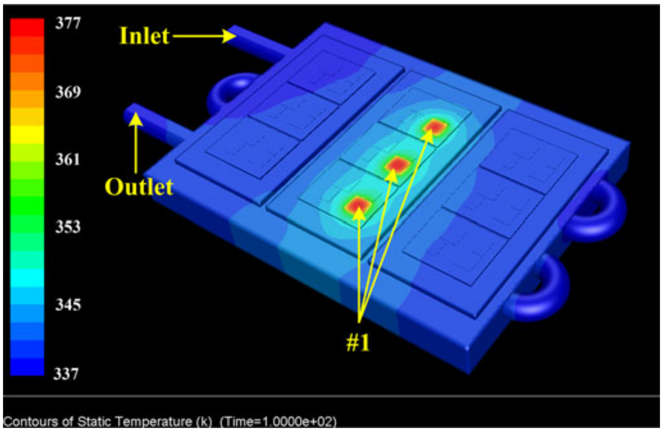

Fig. 5. Temperature distribution at 100 s when the power dissipation is added to the device #1.

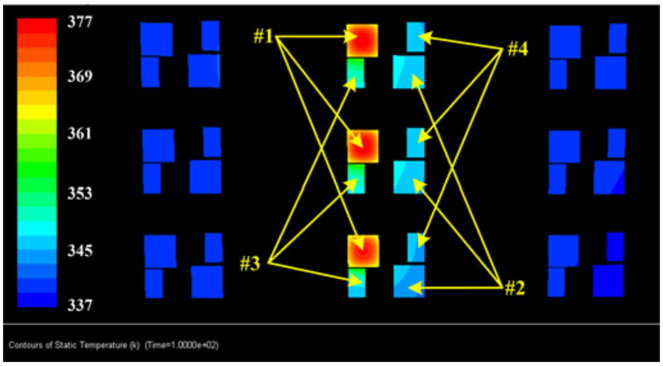

Fig. 6. Temperature distribution of the chips at 100 s when the power dissipation is added to the device #1.

The device #1 in the middle module is heated as an example to illustrate the process. The simulation time is set to 100 s to ensure that the junction temperature reaches the steady state. The temperature field of the cold plate and power modules at 100 s is shown in Fig. 5. The temperature distribution of all the chips is shown in Fig. 6. The temperature rises can be observed at all the chips in the middle module because of the cross-heating effects.

The junction temperature profiles of all the devices are shown in Fig. 7. With the self-heating effect, the device #1 has the maximum junction temperature. Besides, the device #3 is located very close to the device #1. Therefore, it has relatively higher junction temperature. In addition, devices #2 and #3 have similar temperatures because they have the similar distance to the device #1. By using (1), the step response transient thermal impedances can be derived as shown in Fig. 8. It can be found that there is a delay for the cross-heating impedances at the beginning. That is because the chips share the same substrate and base plate, and it takes time for the heat to spread into the adjacent chips.

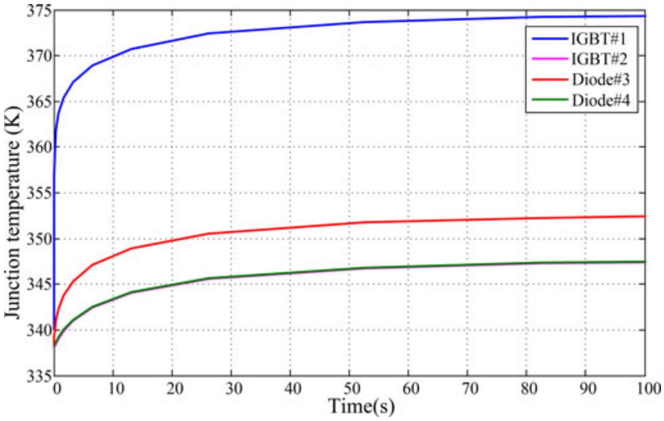

Fig. 7. Junction temperatures of devices when the power dissipation is added to the device #1.

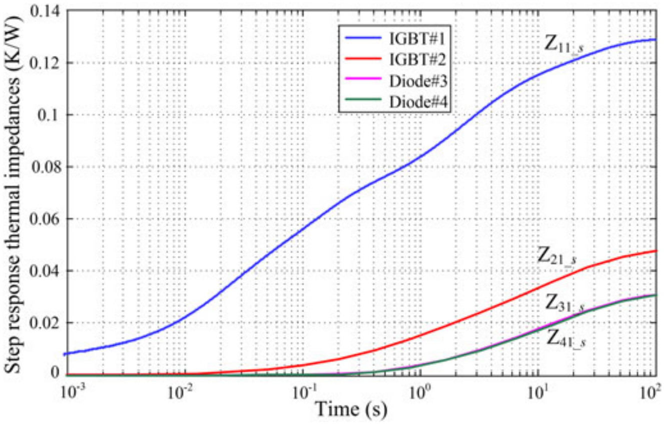

Fig. 8. Step response thermal impedances when the power dissipation is added to the device #1.

TABLE II
OBTAINED PARAMETERS BY HEATING THE DEVICE #1

R_{11_1} (K/W)	R_{11_2} (K/W)	R_{11_3} (K/W)	R_{11_4} (K/W)
0.01201	0.05017	0.03859	0.02732
τ_{11_1} (s)	τ_{11_2} (s)	τ_{11_3} (s)	τ_{11_4} (s)
0.000895	0.051706	1.47167	15.5521
R_{21_1} (K/W)	R_{21_2} (K/W)	R_{31_1} (K/W)	R_{31_2} (K/W)
0.01204	0.01948	0.01771	0.02854
τ_{21_1} (s)	τ_{21_2} (s)	τ_{31_1} (s)	τ_{31_2} (s)
3.72301	24.474	0.628536	13.7533
R_{41_1} (K/W)	R_{41_2} (K/W)	τ_{41_1} (s)	τ_{41_2} (s)
0.01152	0.01806	3.644315	24.1371

These thermal impedance curves are fitted to the step response (6) by using the least square method. The fourth-order and second-order Foster networks are applied to represent the self-heating and cross-heating effects, respectively. The parameters of the thermal impedances are obtained in Table II. This process is repeated four times to obtain all the self-heating and mutual-heating thermal impedances in one power module. With all the impedance parameters, the z-domain form of (3) is applied to calculate the junction temperatures in the processor. There are 16 elements in the matrix of (3), some of which are the same due to the symmetric architecture of the power devices. The simplification of the thermal impedance matrix is included in the future plan in order to speed up the junction temperature calculation.

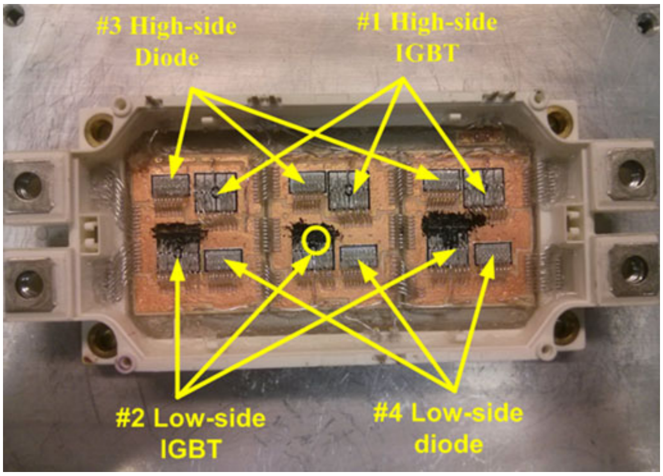

Fig. 9. Location of the thermocouples in the power module.

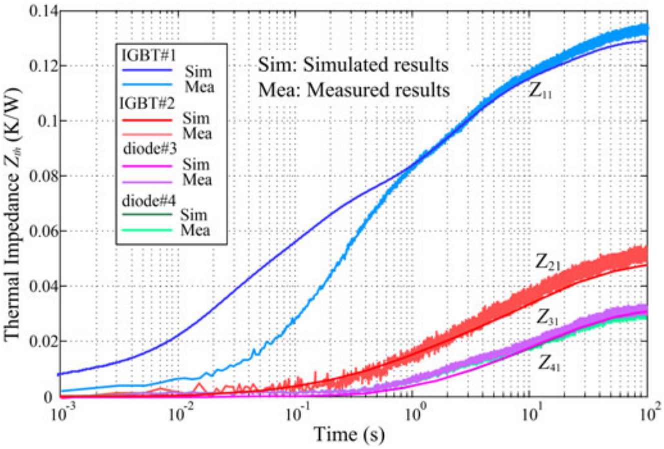

Fig. 10. Comparison of the measured impedances and the simulated results.

C. Experimental Verification of the Thermal Model

In order to verify the accuracy of the developed thermal model, the step response thermal impedance should be measured and compared to the simulation result. Since the junction temperature changes very fast by self-heating, the direct measurement method with thermocouples cannot get the accurate temperature for the self-heating. Therefore, two different methods are applied for the validation: direct temperature measurement for the cross-heating, and the indirect temperature measurement for the self-heating.

The type K Cement-On style 2 (CO2-K) thermocouples from OMEGA is applied for the direct temperature measurement. These thermocouples are made from 0.0005-inch thermocouple alloy foil. First, the gel is carefully removed from the power module to expose the surface of chips, and the location of the thermocouples placed on the IGBTs is demonstrated in Fig. 9 (the yellow circle). Then, a thin layer of OB Epoxy from OMEGA is laid down on the chip surface for insulation (the black coating). After that, the thermocouples are directly bonded to the chip surface covered by the epoxy. These procedures are repeated for the other chips. Comparison of the measured impedances and the simulated results is shown in Fig. 10. It can be found that the error is quite small for the cross-heating (Z_{21}, Z_{31}, and Z_{41}) and, therefore, the accuracy of the thermal model for cross coupling is verified. However, there is a big error for the transient thermal impedance of the self-heating. This is mainly because of the introduced thermal capacitance of the epoxy (the black coating) and the very fast temperature changes.

In order to verify the accuracy of the thermal model for the self-heating, the indirect temperature measurement method is applied by using the TSEP [27]. The voltage across the IGBT (V_{ce}) under small current is applied to measure the junction temperature. The detailed measurement method is described as follows. As shown in Fig. 11, a low constant current I_m is applied to the device under test (DUT) to get the relationship between the junction temperature and voltage drop across the IGBT. Then, the high constant current I_c is applied to the DUT in order to generate the constant power loss. When the power loss is stable, I_c is removed and only I_m is applied during the cooling stage. By recording V_{ce} during the cooling stage and using the relationship between the temperature and V_{ce}, the junction temperature during the cooling stage is obtained. The temperature step response is derived by using the temperature profile during the cooling stage. After the temperature step response is obtained, the step response thermal impedance can be derived. In this paper, the high current source is implemented with the buck converter, and the small current source is implemented by an operational amplifier. The circuit for temperature measurement is shown in Fig. 12. The pulse width modulation (PWM) signal is provided to the switch S_1 to get the desired current to the DUT. When the switch S_2 is ON, the high current is fed to the DUT. The switch S_2 is turned OFF to remove the high-current source. The low-current source provides 1 mA to the DUT to get the relationship between V_{ce} and the junction temperature.

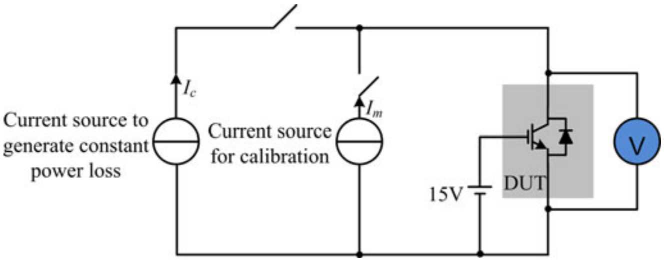

Fig. 11. Principle to measure the junction temperature.

The flow rate is set at 2 L/min, which is the same as the simulation condition. By using this temperature measurement method, the step response thermal impedance of IGBT is obtained. The experimental and simulated thermal impedance curves are plotted in the log axis, as shown in Fig. 13. In contrast to the direct measurement results, the experimental thermal impedance derived from the TSEP is in good accordance with the simulation result in the entire time range. There is a slight error of 3.4% at

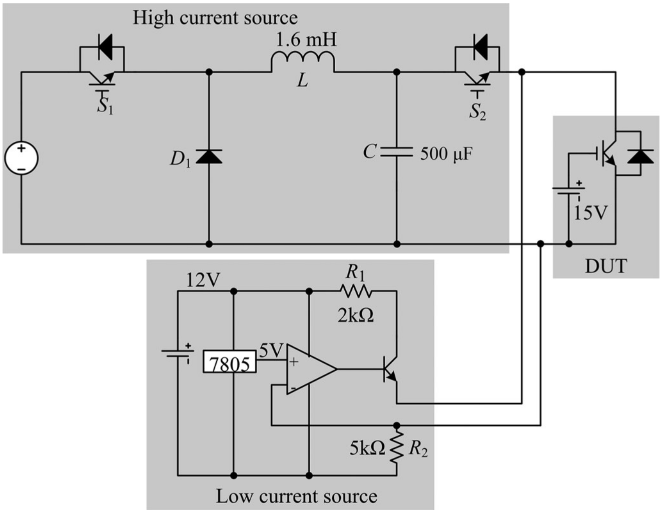

Fig. 12. Circuit schematic for temperature measurement.

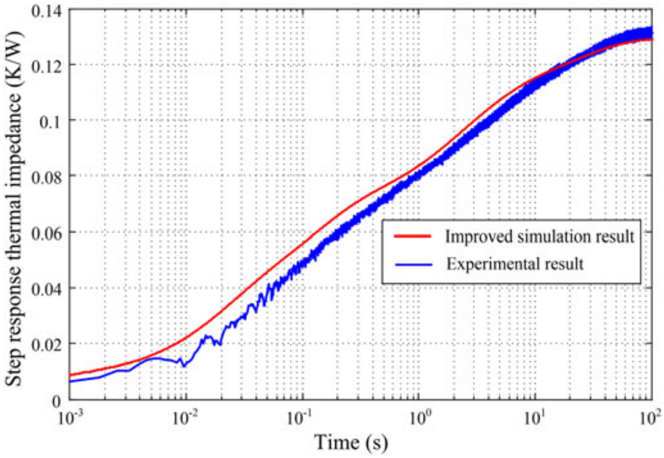

Fig. 13. Improved simulated thermal impedance curve and the experimental curve.

the steady state and 9.7% at the transient state. The error mainly introduced by the following two reasons: 1) the internal dimensions of the power module applied for simulation could not be 100% fit with the reality dimension; 2) the ideal model of the thermal interface material layer between the power module and the cold plate is applied to the simulation, while in reality the thermal grease cannot be uniformly distributed in the contact area. The error is within an accepted level and the self-heating thermal impedance is verified by the experiment.

III. EVALUATION OF THE LINEARITY OF THE THERMAL SYSTEM

The Foster thermal network has been widely used in the thermal modeling of power electronics, and it is based on the linear assumption. However, the real system is not linear in several aspects. First, the thermal performance of the entire system including both the power module and the heat sink are required for power electronics design. Involving the heat sink model will introduce heat convection to the system which is a nonlinear problem. Second, the heat transfer of the inverter is a 3-D thermal spreading process. It will introduce error if the linear assumption is applied. In addition, the thermal properties of materials are temperature dependent and not constant. In this section, the linearity of the heat transfer process for the entire inverter will be investigated. The impact of these nonlinear factors on the accuracy of the linear assumption will be presented.

A. *Verification of the Linear Assumption With Constant Thermal Properties of Materials*

Linear systems have to satisfy two properties, superposition and homogeneity. In this section, these two properties will be verified supposing the thermal properties of materials are constant. The temperature dependency of the thermal model will be investigated in Section III-B.

1) Verification of the Homogeneity: The property of homogeneity states that for a given input x, and for any scalar α in the domain of the function F, (7) is satisfied

$$F(\alpha x) = \alpha F(x). \tag{7}$$

In the thermal model, the input x is the power dissipation, and the output $F(x)$ is the temperature rise. The thermal model of the inverter in ANSYS-Fluent precisely describes the 3-D heat conduction and the heat convection process. Therefore, it is applied to verify the homogeneity of the system. Power dissipation of 30 W per chip and 100 W per chip are added to the system, respectively. The temperature distribution at steady state under different power dissipation conditions are shown in Fig. 14. The comparison of transient thermal impedances under these two power dissipation conditions is shown in Fig. 15. The thermal impedances have only 1.6% difference in the steady state. This system can be assumed to meet the homogeneity property. The larger power dissipation will lead to the larger temperature difference between the power device and coolant, and then to the larger heat spreading area. The larger heat spreading area will make the heat convection more efficient, which will help reduce the thermal impedance. The thermal impedance, which is reversely proportional to the heat spreading area, will be also reduced due to the larger heat spreading area. Therefore, the thermal impedance at 300 W is slightly smaller than at 90 W due to the larger power dissipation as shown in Fig. 15.

2) Verification of the Superposition: The superposition states that for different inputs x_i, in the domain of the function F, (8) should be satisfied

$$F(x_1 + x_2 + \cdots + x_n) = F(x_1) + F(x_2) + \cdots + F(x_n) \tag{8}$$

x_i is the power loss, and $F(x_i)$ is the temperature rise. There are four independent heat sources in one power module: device #1, device #2, device #3, and device #4. As an example, the temperature rise of device #1 is considered when 100 W power dissipation is added to different devices. $F(x_i)(i = 1, 2, 3,\ \text{and}\ 4)$ is the temperature rise of device #1 when the 100 W is added to device #*i*. Transient thermal simulation is conducted to get these temperature profiles. Then, power dissipations with various values are added to all the devices simultaneously, as shown in Fig. 16. Compared to the single heat source, the input of

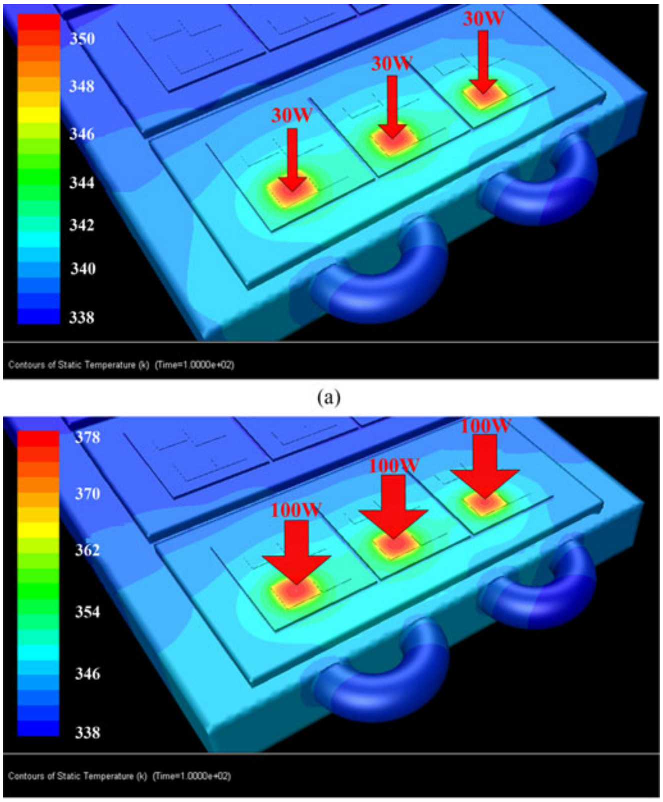

(a)

(b)

Fig. 14. Temperature distribution with different power dissipation: (a) with 90 W, (b) with 300 W.

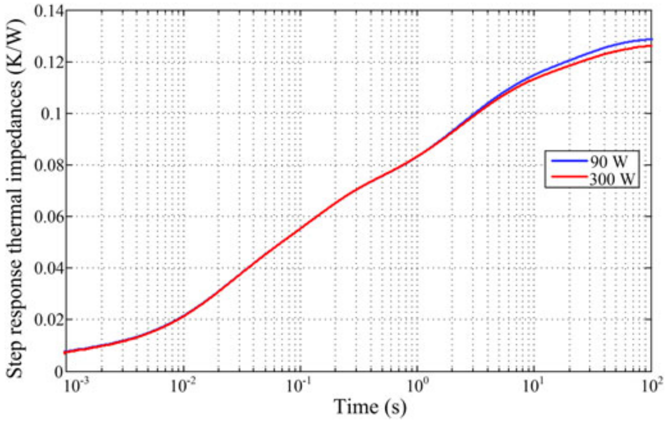

Fig. 15. Step response thermal impedance curves with 90 W and 300 W power dissipations.

the system becomes $3 * x_1 + 2 * x_2 + 1.5 * x_3 + 1 * x_4$, if the system satisfies the superposition, the temperature rise of device #1 $F(3 * x_1 + 2 * x_2 + 1.5 * x_3 + 1 * x_4)$ should be equal to $3 * F(x_1) + 2 * F(x_2) + 1.5 * F(x_3) + 1 * F(x_4)$. The temperature rise curves are obtained as shown in Fig. 17. It can be found that the temperature rise due to multiple heat sources is slightly smaller than that obtained by superposition. This is because the thermal impedance due to multiple heat sources is slightly smaller than that due to the single heat source. With multiple heat sources, the heat spreads more widely on the cold plate, which increases regions with the temperature difference. Then, the heat convection between the cold plate and the coolant becomes more efficient, which in turn reduce the thermal impedance with multiple heat sources. However, the error is within 2%, as shown in Fig. 17. Therefore, the system can also be assumed to meet the superposition property. According to the verification, the thermal model of the entire inverter satisfies both the properties of homogeneity and superposition. It can be assumed as a linear system if the temperature-dependent thermal properties of material are not considered. It should be noted that the coolant flow of this typical inverter in electrified vehicles is in the laminar condition or early stage of the transition between the laminar and turbulence. Therefore, the linearity of the heat convection is guaranteed. However, the nonlinear behavior is more obvious in very high power applications using some advanced cooling methods. For example, the phase change spray cooling is being used in some utility-scale applications.

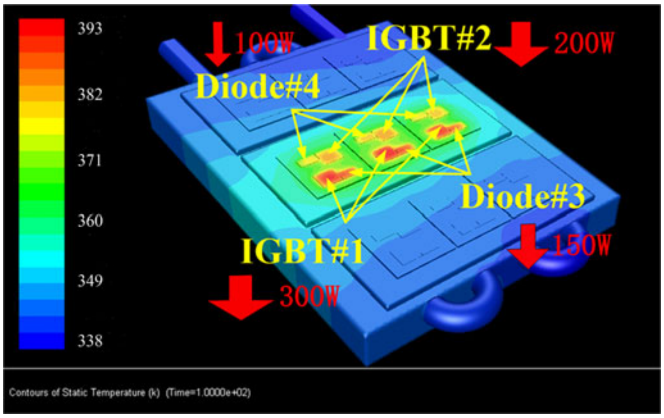

Fig. 16. Temperature rise distribution when all the devices are heated.

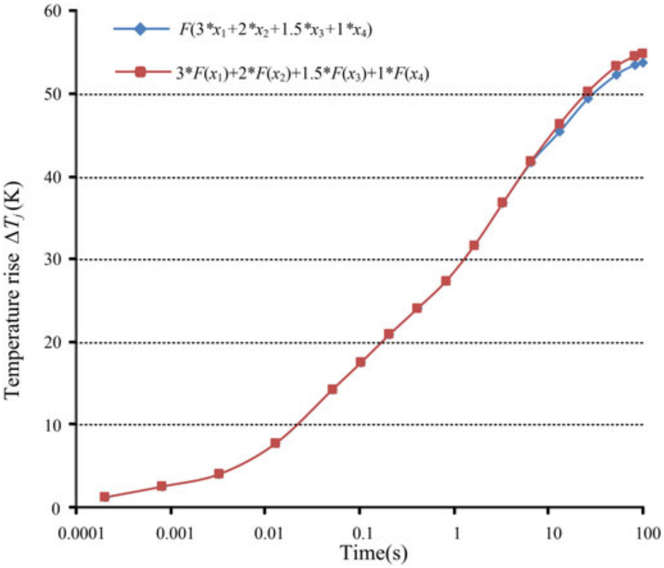

Fig. 17. Curves of temperature rise.

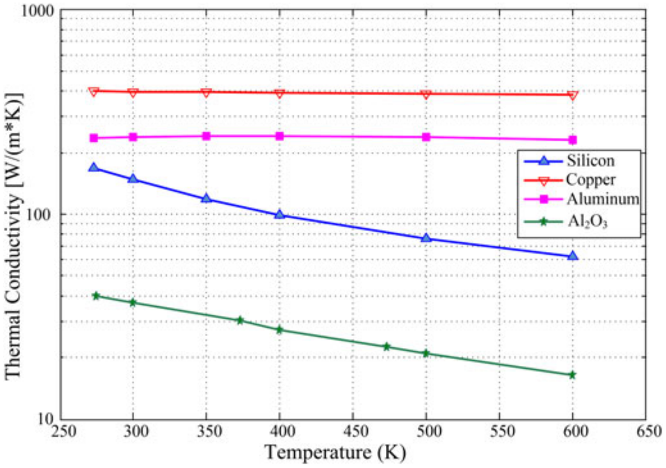

Fig. 18. Temperature-dependent thermal conductivities of materials [32].

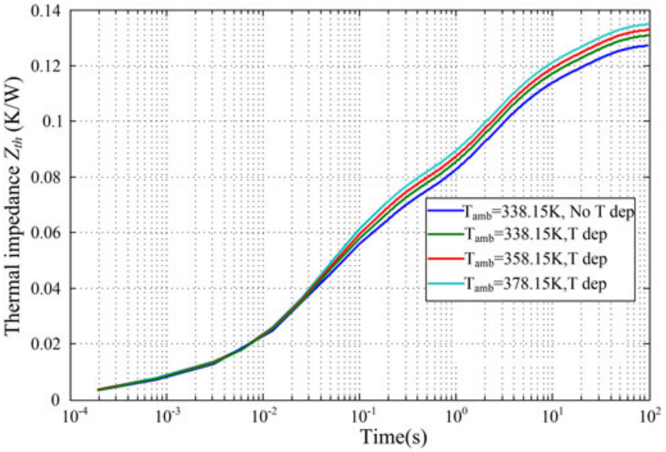

Fig. 19. Thermal impedance curves under different ambient temperatures.

The linearity of these systems needs to be verified before using the linear thermal modeling method.

B. Temperature Dependency of the Thermal Model

There are mainly three reasons leading to the nonlinearities in the thermal model: the heat spreading effects, the heat convection process, and the temperature dependence of the material properties. The first two factors have been evaluated, and the last factor will be discussed in this section.

1) Temperature Dependence of the Materials: The impact of the temperature-dependent thermal properties on the thermal model is controversial in the previous literature. It is ignored in [28], [29] while errors from 4% to 12% caused by using temperature-independent assumption are reported in [22] and [30]. There are two thermal properties of materials, thermal conductivity λ and heat capacity $C_{\rm th}$. The temperature dependence of heat capacity can be negligible in the 0 °C –150 °C range [31]. Therefore, the thermal conductivity is the primary factor which may result in the nonlinearity. Thermal conductivities of materials vary significantly over a wide temperature range. The power semiconductors operate in a range of 250–450 K, which is the temperature of interest in this paper. Fig. 18 shows the temperature dependence of the thermal conductivities of materials in a power module [32]. Aluminum and copper show the minor temperature dependence of λ. Only the thermal conductivities of silicon and Al_2O_3 vary significantly at the temperature of interest.

2) Influence on the Thermal Model: In order to evaluate the errors caused by neglecting the temperature dependence of thermal properties, a full nonlinear CFD model is built in ANSYS-Fluent with the temperature-dependent thermal conductivity of materials in Fig. 19. The transient simulation is repeated by gradually increasing ambient temperatures from 338.15 K (65 °C) to 378.15 K (105 °C), which is the typical coolant temperature range of the cooling for power converters in electrified vehicles. A comparison between the linear model and the nonlinear model with different ambient temperatures is shown in Fig. 19. “$T_{\rm amb}$= 338.15 K, No T dep” in the legend indicates that the constant thermal conductivity of material at 338.15 K is applied to the simulation. The “T dep” indicates that the temperature-dependent thermal conductivity is used.

As shown in Fig. 19, as the ambient temperature rises, the thermal conductivities of both Al_2O_3 and silicon reduces and, therefore, the thermal impedance increases. Compared to the linear model with a constant thermal conductivity at 338.15 K (the curve with the legend “$T_{\rm amb}$ = 338.15 K, No T dep”), the error due to the temperature dependence of thermal conductivity is around 7% when the ambient temperature is set to 378.15 K (the curve with the legend “$T_{\rm amb}$ = 378.15 K, T dep”). Therefore, if the constant thermal conductively at 338.15 K is applied, the largest error is around 7% at 100 s by considering the worst case. The thermal impedance error is mainly introduced by the variation of the thermal conductivity of Al_2O_3 rather than the variation of the thermal conductivity of silicon. It is because the area and thickness of the silicon layer are much smaller than those of the Al_2O_3 layer, and the thermal conductivity of silicon is much larger than that of the Al_2O_3. Therefore, the thermal resistance of the silicon layer takes up only a small fraction of the thermal resistance of the whole thermal system, and its impact on the entire thermal system is negligible.

There are no perfect solutions in these cases. In literature [32], the average thermal impedance at different temperatures is applied to solve this issue. A method to generate a temperature-dependent physical-based thermal network model is proposed by simplifying the power module model from at least seven layers to four layers, which reduces the model accuracy to some extent. In this paper, a simple thermal modeling method is proposed considering the temperature-dependent thermal conductivity. The temperature range of the materials in the power module is most likely to be known when the inverter is operating. For instance, the optimal junction temperature and the lowest coolant temperature are 423.15 K (150 °C) and 338.15 K (65 °C), respectively. The average of these two values is 380.65 K (107.5 °C). In this paper, the thermal conductivity of all the materials at this average temperature is used to build the thermal model. A comparison of this proposed simplified model and the full temperature-dependent model with the coolant inlet

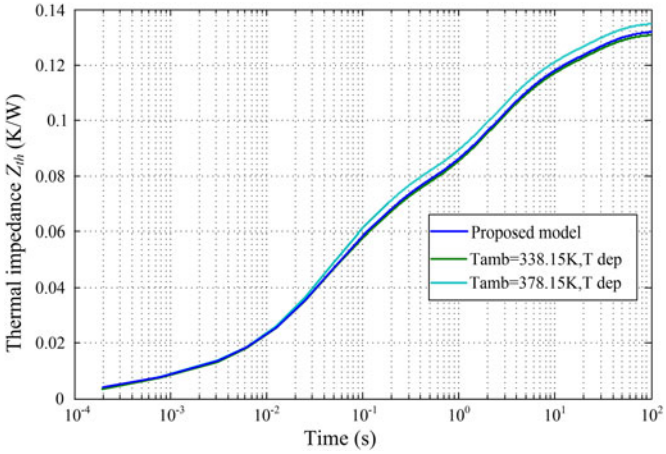

Fig. 20. Thermal impedance curves with the proposed model and the temperature-dependent model.

temperature at 338.15 and 378.15 K is shown in Fig. 20. Compared to the worst case (the curve with the legend "$T_{\mathrm{amb}} = 378.15$ K, T dep"), the error is around 2% at 100 s. Therefore, with the proposed thermal modeling method, the error in the worst case can be reduced from around 7% to 2%. Besides, the temperature-dependent nonlinear model, which is very time-consuming, is avoided by using the proposed method.

IV. TEMPERATURE-DEPENDENT POWER LOSS MODEL

Since the switching frequency is much higher than the crossover frequencies of the thermal impedances, the average power losses during a switching cycle can be applied to estimate the junction temperatures. In order to reduce the simulation time, two following assumptions are made: 1) the load current ripple is ignored; 2) the conductive current is constant during a switching cycle. The curve fitted functions are applied to obtain the voltage drops of devices.

A. Conductive Loss

The instantaneous conductive loss of IGBT or diode is obtained by using the multiplication of voltage drop and the conductive current, as shown in

$$p_{\mathrm{cond}} = v(t) \times i(t) \tag{9}$$

where $v(t)$ is the voltage drop of device and $i(t)$ is the conductive current.

Assuming that the conductive current is constant during a switching cycle, the average conductive losses of the IGBT and the diode over a switching cycle are represented as

$$P_{c\_\mathrm{igbt}} = \frac{V_{ce} I_c t_i}{T_s} \tag{10}$$

$$P_{c\_\mathrm{diode}} = \frac{V_F I_D t_d}{T_s} \tag{11}$$

where P_{c_igbt} and P_{c_diode} are the average power losses of the IGBT and the diode over a switching cycle, respectively; V_{ce} is the voltage drop of the IGBT when the conductive current is I_c; V_F is the forward voltage drop of the diode when the conductive current is I_D; t_i and t_d are the conduction time of the IGBT and diode during a switching period, respectively.

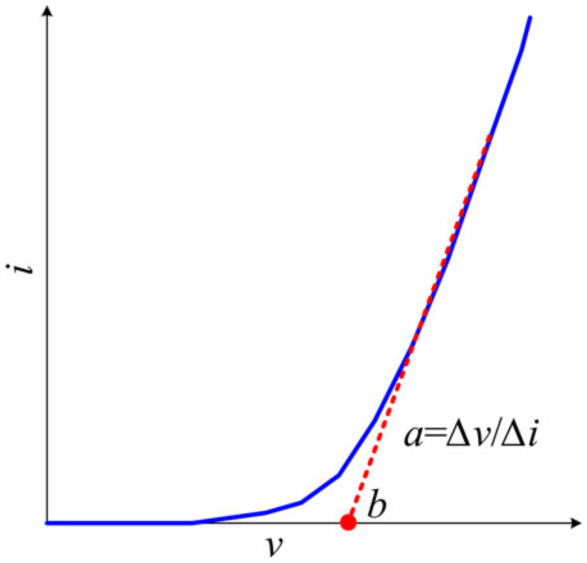

Fig. 21. Voltage drop of power device.

For a given temperature, the voltage drop of IGBT or diode at different conductive currents has the shape shown in Fig. 21. Here, the voltage drop is approximated as a function shown in

$$v(t) = a \cdot i(t) + b. \tag{12}$$

In order to represent the temperature effects on the power losses, the coefficients a and b in (12) are assumed to be linear functions of the junction temperature. Their respective expressions are given in

$$\begin{aligned} a &= a_0 + r_1(T_j - T_0) \\ b &= b_0 + r_2(T_j - T_0) \end{aligned} \tag{13}$$

where a_0 and b_0 are the coefficients when the junction temperature equals to the nominal temperature T_0; r_1 and r_2 represent the temperature sensitivity of these coefficients.

B. Switching Loss

The switching energy dissipation is sensitive to the stray inductance of the dc-link and the gate resistance. Although the switching energy dissipations under different junction temperatures and currents are provided in the datasheet of power devices, the circuit parameters of practical traction inverter are always different from the test conditions listed in the datasheet. In order to get the accurate switching loss, double-pulse test experiments are conducted. The turn-on and turn-off waveforms of IGBT are shown in Fig. 22. The green, yellow, and blue waveforms are the gate signal V_{ge}, current I_c, and the voltage across the IGBT V_{ce}, respectively. The voltage output of the Rogowski coil is 0.01 V/A. The measured voltage by using the coil is 4 V when the switch is turned OFF. Therefore, the current is 400 A. By multiplying the voltage and current waveforms during the switching

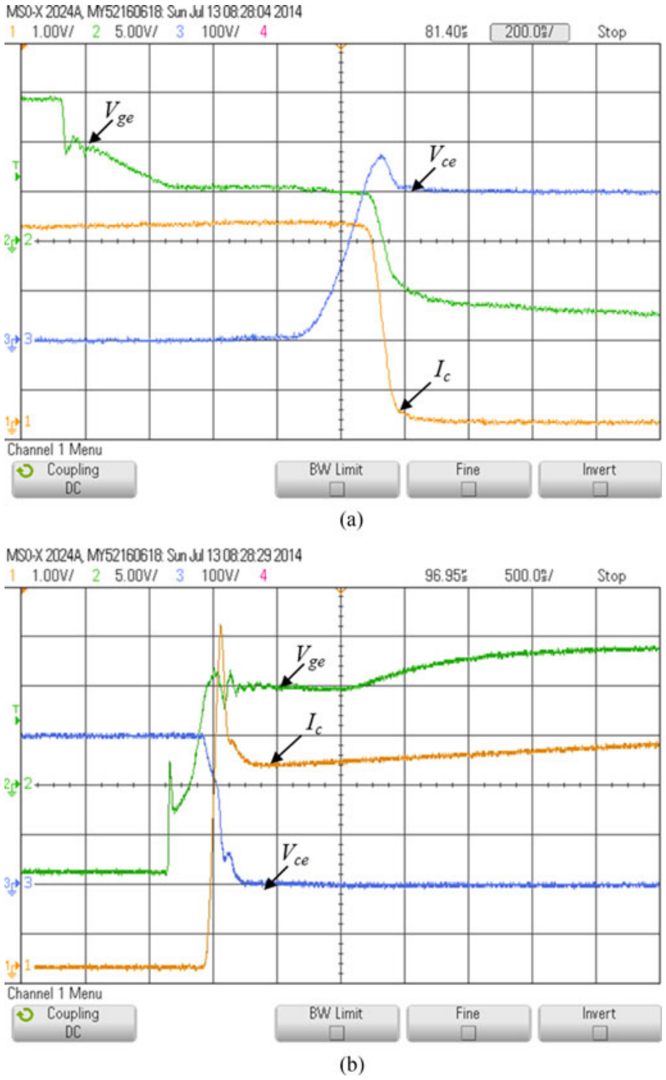

(a)

(b)

Fig. 22. Turn-on and turn-off waveforms of IGBT. (a) Turn-off waveforms and (b) turn-on waveforms (300-V dc-link, 400 A current, and 25 °C temperature).

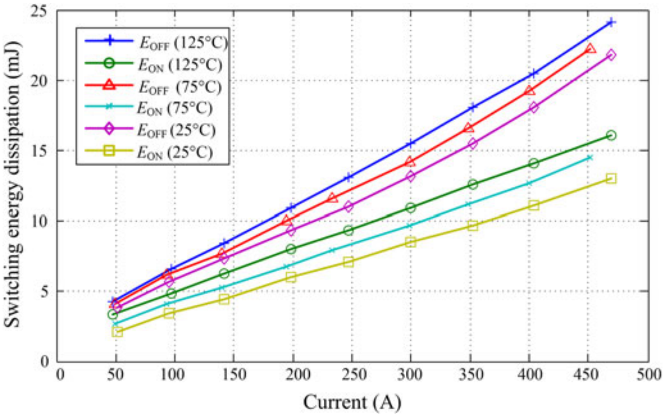

Fig. 23. Switching energy dissipation of IGBT with 300-V dc-link voltage.

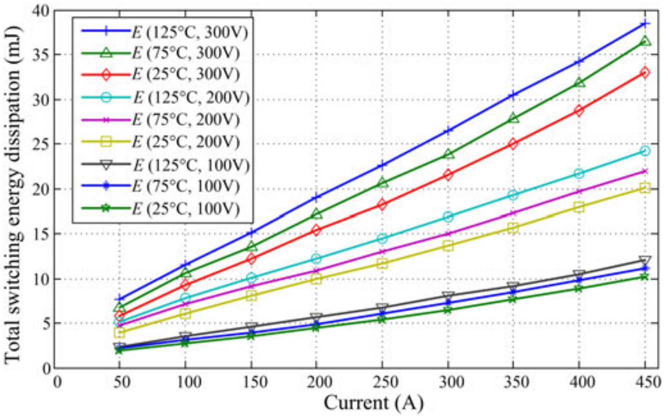

Fig. 24. Total switching energy dissipation of IGBT under different conditions.

process, the switching energy dissipation is obtained. Similarly, the reverse recovery energy dissipation is measured.

With dc-link voltage 300 V, the obtained switching energy dissipations of IGBT under different currents and junction temperatures are plotted in Fig. 23. E_{OFF} and E_{ON} denote turn-off and turn-on switching energy dissipation, respectively. The switching energy dissipation increases as junction temperature increases. The switching energy dissipation is a function of the dc-link voltage, the current, and the junction temperature. Therefore, four-dimensional lookup tables are required to get the switching loss, which is complicated and requires a lot of computational resources. In order to simplify the lookup table, the total switching energy dissipation under different voltages, currents, junction temperatures are investigated. The total switching energy dissipations are plotted in Fig. 24. Under the same current and temperature, it can be found that the switching energy dissipation is approximately proportional to the dc-link voltage. For example, at 25 °C, the total switching energy dissipation at 300 V is around three times as that at 100 V. Therefore, the 3-D lookup table with 300-V dc-link voltage can be applied to calculate the switching loss. The total energy dissipations of IGBT at dc-link voltage V_{dc} can be calculated by multiplying the obtained energy dissipation at 300 V with the coefficient $V_{\mathrm{dc}}/300$. Similarly, the obtained reverse recovery energy dissipations E_{rec} under 300 V are shown in Fig. 25. The reverse recovery energy dissipation of diode at dc-link voltage V_{dc} can be calculated by multiplying the obtained E_{rec} at 300 V with the coefficient $V_{\mathrm{dc}}/300$. Therefore, by using the lookup table shown in Fig. 25, E_{rec} at different dc-link voltages is obtained. By using the measured switching energy dissipations, the average switching loss of the IGBT and the diode can be represented as

$$P_{s\_\mathrm{igbt}} = \frac{E_{\mathrm{ON}} + E_{\mathrm{OFF}}}{T_s} \tag{14}$$

$$P_{s\_\mathrm{diode}} = \frac{E_{\mathrm{rec}}}{T_s} \tag{15}$$

where P_{s_igbt} and P_{s_diode} are the switching power losses of the IGBT and the diode, respectively, T_s is the switching period.

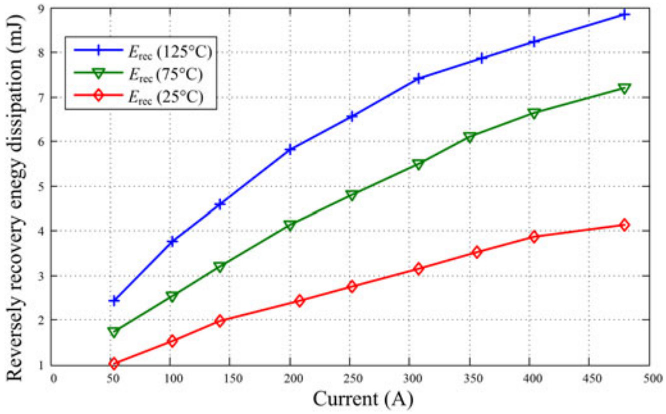

Fig. 25. Reverse recovery energy dissipation of diode with 300-V dc-link voltage.

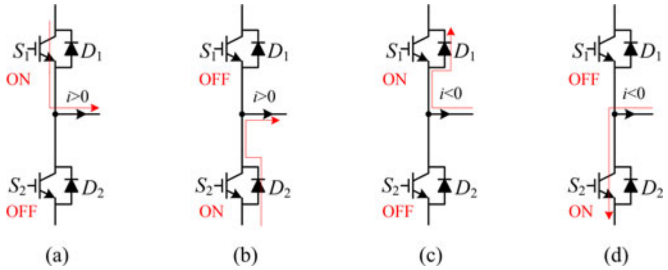

Fig. 26. Current flow under different driver signals and load current directions. (a) S_1 is ON and $i > 0$, (b) S_2 is ON and $i > 0$, (c) S_1 is ON and $i < 0$, (d) S_2 is ON and $i < 0$.

C. Total Loss

The gate drive signals and the load current direction determine which device in a phase leg conducts the load current, as shown in Fig. 26. If S_1 is ON and the load current is positive, S_1 is conducted; if S_2 is ON and the load current is positive, D_2 is conducted; if S_1 is ON and the load current is negative, D_1 is conducted; if S_2 is ON and the load current is negative, S_2 is conducted. The processor of the inverter derives the required duty cycle for the power devices to control the torque or speed of the electric machine. According to Fig. 26 and the direction of the load current, the processor can judge which device is carrying the current. Because the duty cycle is also known to the processor and, therefore, the average conductive losses of the devices can be derived by using (10)–(13). For instance, if the duty cycle of the S_1 is *d* and the load current is positive ($i > 0$), as the conditions shown in Fig. 26(a) and (b), the average conductive loss of IGBT S_1 and D_1 shown in (10) and (11) become $V_{ce} I_c d$ and $V_F I_D (1{-}\mathrm{d})$, respectively. In addition, the average switching loss can be obtained by using the lookup tables and (14) and (15). When the average conductive and switching losses are obtained, the average power losses of the IGBT P_I and the diode P_D for a switching cycle are represented as

$$P_I = P_{c\_\mathrm{igbt}} + P_{s\_\mathrm{igbt}} \tag{16}$$

$$P_D = P_{c\_\mathrm{diode}} + P_{s\_\mathrm{diode}}. \tag{17}$$

TABLE III
SIMULATION PARAMETERS FOR POWER LOSS PROFILES

DC-link voltage	300 V	Fundamental frequency	50 Hz
Modulation method	SVPWM	Load resistance *R*	0.5 Ω
Modulation index	0.8	Load inductance *L*	0.5 mH

V. DETERMINATION OF CALCULATION RATE FOR THE FAST ELECTRO-THERMAL MODEL

As presented in Section II, many calculation steps are required to obtain the junction temperatures of all power devices. If a long real-time simulation is required, such as drive cycles, the computational time would be very long and the memory resources may be not enough. Therefore, the proper calculation rate for junction temperature estimation should be determined to reduce the computational time while keeping the required accuracy of the estimated junction temperatures. The junction temperature estimation includes two parts: power loss estimation and the thermal model of traction inverter. Therefore, the calculation rate of junction temperature estimation is determined by both the power loss profiles and properties of thermal impedance.

A. Calculation Rate Considering Power Loss Profiles

A simulation of traction inverter with *RL* load is conducted to get the power loss profile of each device. The simulation circuit parameters are listed in Table III. The power loss properties of power module FF600R06ME3 from Infineon are applied for the simulation, and the switching frequency is set to 10 kHz. The derived power loss lookup table in Section IV is applied to get the switching cycle-based average losses. The average power losses of devices in a phase leg are obtained by using Matlab simulation, and they are shown in Fig. 27. It can be found that the power loss profiles are similar to the half-sinusoidal waveforms. As shown in Fig. 28, the dominant harmonics of power loss profiles are the first and second orders.

The Nyquist–Shannon sampling theorem presents that a band-limited function can be reconstructed if the band limit is smaller than half of the sampling rate. If the theorem is not satisfied, the spectrum of sampled sequence is different from that of the original function, and this phenomenon is defined as Aliasing. If the calculation rate for junction temperature estimation can meet the Nyquist–Shannon sampling theorem, the aliasing can be avoided. Unfortunately, the power loss profiles are not band-limited signals and, therefore, there is always aliasing with any calculation rates. However, if the calculation rate is higher than the two times of the maximum dominant harmonics of power loss profiles, severe aliasing can be avoided, and the power loss profiles can be obtained with high accuracy. Since the maximum dominant harmonics of power loss profiles is the second order, the calculation rate should be set to two times as higher as the second order. If the calculation rate and maximum fundamental frequency of the electric traction machine are denoted as f_{cal} and f_1, respectively, the calculation rate should

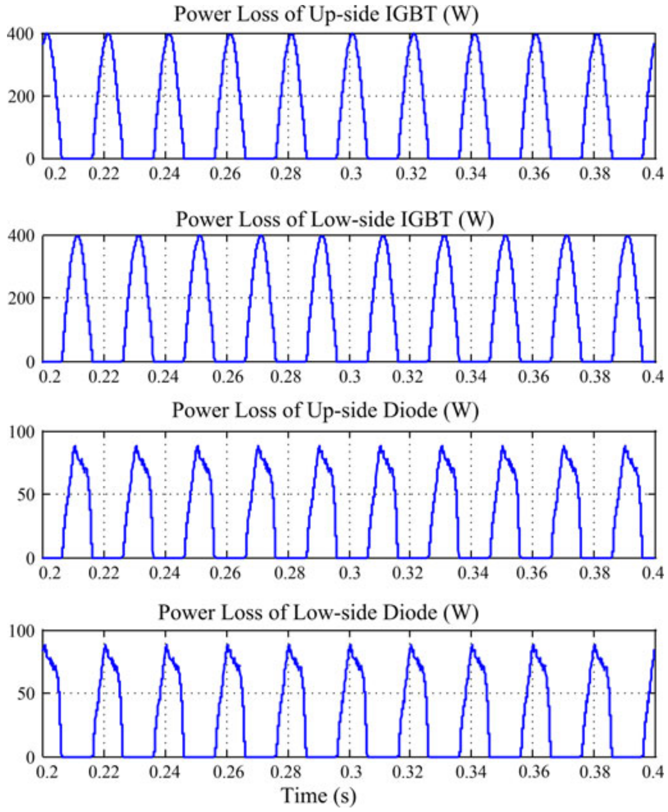

Fig. 27. Power loss profiles of each devices in a phase leg.

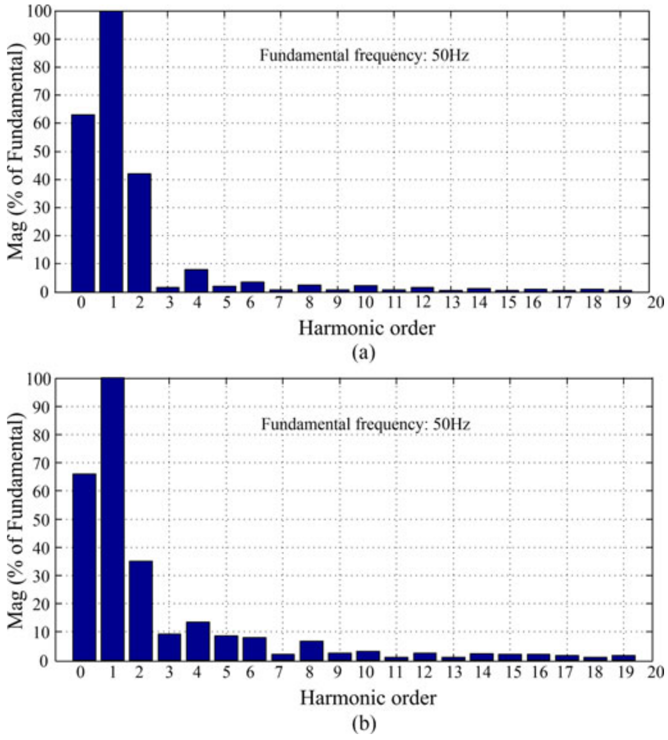

Fig. 28. Spectrums of power losses of IGBT and diode. (a) IGBT. (b) Diode.

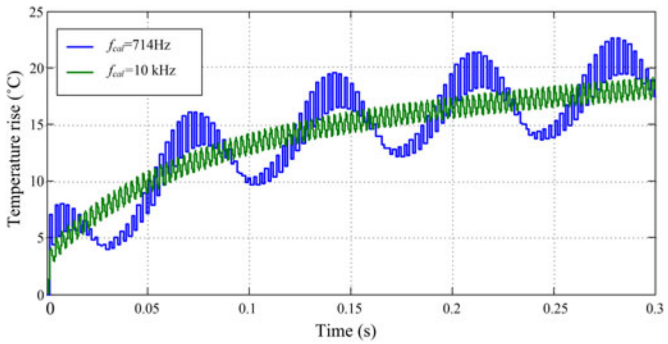

Fig. 29. Temperature rise with $f_{\mathrm{cal}} = 714$ Hz and $f_{\mathrm{cal}} = 10$ kHz (benchmark for comparison).

meet the constraint

$$f_{\mathrm{cal}} > 4f_1. \tag{18}$$

Taking the Prius 2004 HEV as an example, the maximum fundamental frequency of the electric traction machine f_1 is around 350 Hz with vehicle speed 150 km/h. Considering this worst case and the calculation rate constraint of (18), the calculation rate f_{cal} have to be higher than 1400 Hz to avoid the severe aliasing. In order to verify this calculation rate constraint, electro-thermal simulations are conducted by using the derived thermal impedance in Section II and the measured power loss lookup table in Section IV. The developed electro-thermal model is implemented in the M-file of the Matlab. The simulation parameters are the same as Table III except that the fundamental frequency is set to 350 Hz. Two cases of the simulation are conducted for the comparison: 1) $f_{\mathrm{cal}} = 714$ Hz (every 14 switching cycles), which is lower than 1400 Hz and violates the constraint of (18); 2) $f_{\mathrm{cal}} = 1429$ Hz (every seven switching cycles), which is higher than 1400 Hz and can meet the constraint of (18). Also, electro-thermal simulation with 10 kHz calculation rate is conducted. It calculates the power loss and junction temperature at every switching cycle, and the result is close to the actual temperature profile. Therefore, the temperature profile with 10 kHz calculation rate is regarded as the benchmark for the accuracy comparison.

Fig. 29 shows the temperature rise of the simulation case 1. It can be found that the profile with 714 Hz calculation rate is far away from the result obtained with 10 kHz calculation rate. The calculation rate cannot satisfy the constraint of (18), and the severe error is introduced because of the severe aliasing phenomenon. For comparison, Fig. 30 shows the temperature rise of the simulation case 2. Because the calculation rate can meet the constraint of (18), a very slight error can be found between the results obtained with 1429 Hz and 10 kHz. Instead of calculating the power loss and the junction temperatures of devices at every switching cycle, these calculations can be conducted at every seven switching cycles, and it can still guarantee the accuracy. It means that the power losses and junction temperatures are calculated every seven switching cycles instead of each switching cycle, which can significantly improve the speed of the electro-thermal simulation. According to these simulation results, the derived calculation rate constraint is verified.

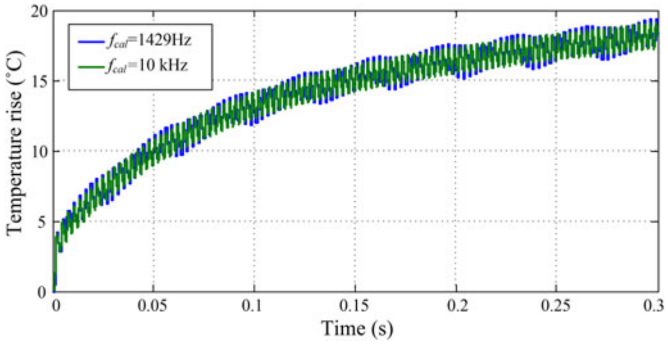

Fig. 30. Temperature rise with $f_{\text{cal}} = 714$ Hz and $f_{\text{cal}} = 10$ kHz (benchmark for comparison).

It should be noted that the 350 Hz small temperature variation in Fig. 30 is generated by the fundamental frequency power loss variation. Because the fundamental frequency is relatively higher compared to thermal impedance corner frequency, the fundamental frequency variation is small.

B. Calculation Rate Considering the Properties of Thermal Impedance

In the stand-still operation mode of the electric traction machine, huge dc current goes through partial of the power devices and junction temperatures are raised very rapidly due to the large constant power loss and small thermal capacitance of silicon die. If the calculation rate is set very low, massive errors would be introduced between the actual and estimated temperature rise and, therefore, the overtemperature protection cannot be implemented in time. In this section, the impact of calculation rate on the maximum error of estimated junction temperature is analyzed.

The temperature rise produced by the self-heating is much faster than that produced by thermal coupling because the time constant of thermal impedance for thermal coupling is relatively larger. Therefore, just the self-heating is considered for the analysis of maximum error of estimated junction temperature. The temperature rise of IGBT #1 can be represented as (19) by using the obtained parameters shown in Table II and constant power loss P

$$\Delta T(t) = P\begin{bmatrix} R_{11\_1}(1-e^{-t/\tau_{11\_1}}) + R_{11\_2}(1-e^{-t/\tau_{11\_2}}) \\ +R_{11\_3}(1-e^{-t/\tau_{11\_3}}) + R_{11\_4}(1-e^{-t/\tau_{11\_4}}) \end{bmatrix}. \tag{19}$$

The derivative of the temperature rise is derived as

$$\begin{aligned} \frac{d\Delta T(t)}{dt} &= P\left(\frac{R_{11\_1}}{\tau_{11\_1}}e^{-t/\tau_{11\_1}} + \frac{R_{11\_2}}{\tau_{11\_2}}e^{-t/\tau_{11\_2}}\right. \\ &\quad \left. + \frac{R_{11\_3}}{\tau_{11\_3}}e^{-t/\tau_{11\_3}} + \frac{R_{11\_4}}{\tau_{11\_4}}e^{-t/\tau_{11\_4}}\right). \end{aligned} \tag{20}$$

The maximum derivative of the temperature rise is derived as

$$\frac{d\Delta T(t)}{dt}|_{t=0} = P\left(\frac{R_{11\_1}}{\tau_{11\_1}} + \frac{R_{11\_2}}{\tau_{11\_2}} + \frac{R_{11\_3}}{\tau_{11\_3}} + \frac{R_{11\_4}}{\tau_{11\_4}}\right). \tag{21}$$

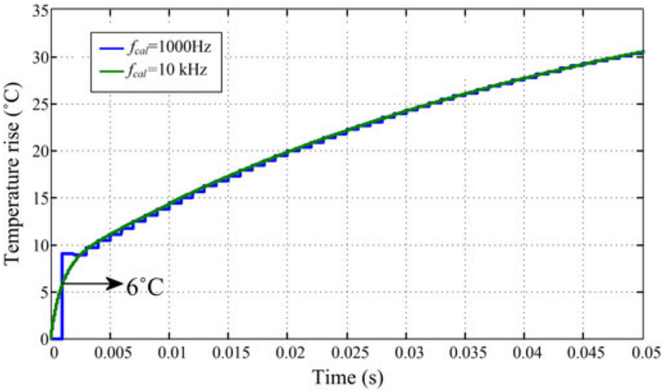

Fig. 31. Temperature rise with $f_{\text{cal}} = 1000$ Hz and $f_{\text{cal}} = 10$ kHz (benchmark for comparison).

If the calculation interval is denoted as Δt, the maximum error of the estimated junction temperature $T_{\text{err\_max}}$ is obtained as

$$T_{\text{err\_max}} \approx P\left(\frac{R_{11\_1}}{\tau_{11\_1}} + \frac{R_{11\_2}}{\tau_{11\_2}} + \frac{R_{11\_3}}{\tau_{11\_3}} + \frac{R_{11\_4}}{\tau_{11\_4}}\right)\Delta t. \tag{22}$$

With specific constant power loss P and maximum temperature estimation error $T_{\text{err\_max}}$, the calculation interval is derived as

$$\Delta t \approx \frac{T_{\text{err\_max}}}{P\left(\frac{R_{11\_1}}{\tau_{11\_1}} + \frac{R_{11\_2}}{\tau_{11\_2}} + \frac{R_{11\_3}}{\tau_{11\_3}} + \frac{R_{11\_4}}{\tau_{11\_4}}\right)}. \tag{23}$$

Therefore, calculation rate is represented as

$$f_2 = \frac{P\left(\frac{R_{11\_1}}{\tau_{11\_1}} + \frac{R_{11\_2}}{\tau_{11\_2}} + \frac{R_{11\_3}}{\tau_{11\_4}} + \frac{R_{11\_4}}{\tau_{11\_4}}\right)}{T_{\text{err\_max}}}. \tag{24}$$

If the required error of estimated temperature is smaller than the specific value $T_{\text{err\_max}}$, the calculation rate f_{cal} has to meet the requirement

$$f_{\text{cal}} > f_2. \tag{25}$$

Simulation is conducted to verify (25). Assuming $P = 675$ W and $T_{\text{err\_max}} = 5$ °C, the calculation rate f_2 is calculated as 1819 Hz according to (24). Two different calculation rates are simulated for comparison: one is $f_{\text{cal}} = 1000$ Hz (every ten switching cycles) and the other one is $f_{\text{cal}} = 2000$ Hz (every five switching cycles). Similar to Section V-A, the result with $f_{\text{cal}} = 1000$ kHz is applied as the benchmark for the comparison. Fig. 31 shows the temperature rise with calculation rate 1000 Hz. It can be found that the maximum estimation error is 6 °C, which is higher than the desired value. It is mainly because that the calculation rate cannot meet the requirement (25). Fig. 32 shows the temperature rise with calculation rate 2000 Hz. Since the calculation rate can meet (25), the maximum estimation error is 3.5 °C, which is smaller than $T_{\text{err\_max}}$.

Considering the requirements of calculation rate shown in (18) and (25), the calculation rate can be selected as (26) to speed up the calculation

$$f_{\text{cal}} = \max(4f_1, f_2). \tag{26}$$

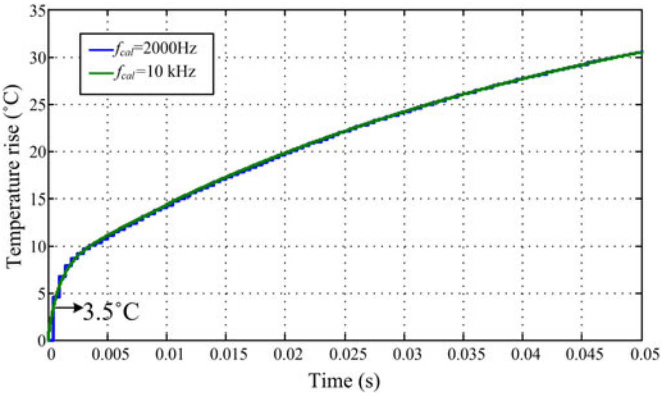

Fig. 32. Temperature rise with $f_{\mathrm{cal}} = 2000$ Hz and $f_{\mathrm{cal}} = 10$ kHz (benchmark for comparison).

VI. Conclusion

In this paper, a fast electro-thermal model is proposed for the traction inverters in electrified vehicles. The linear assumption based thermal modeling method is applied to the thermal model of the entire inverter. The impact of the thermal spreading effect, heat convection, and temperature-dependent material thermal properties on the linear assumption is investigated by ANSYS-Fluent simulation. It is concluded that the thermal spreading effect and heat convection have introduced a negligible error to the linear thermal model. However, the temperature-dependent thermal conductivity of $\mathrm{Al_2O_3}$ can introduce relatively larger errors to the thermal model at room temperature. In order to reduce the error due to the temperature-dependent conductivity, the thermal conductivity at the average temperature of the possible material temperature range is applied in this paper. With the proposed method, the error introduced by the temperature-dependent thermal conductivity can be improved from around 7% to 2%. Besides, a method to determine the calculation rate is proposed by considering both the properties of the thermal model and power loss profile. With the proposed method, it is unnecessary to calculate the power losses and junction temperatures of power devices for every switching cycle. Instead, the junction temperature can be calculated for more than every five switching cycles while keeping the required accuracy. Therefore, the proposed method can significantly reduce the computational burden, which is vital to long-time simulation needed for electrified vehicles.

References

[1] H. Wang, M. Liserre, and F. Blaabjerg, “Toward reliable power electronics: Challenges, design tools, and opportunities,” *IEEE Ind. Electron. Mag.*, vol. 7, no. 2, pp. 17–26, Jun. 2013.

[2] H. Wang *et al.*, “Transitioning to physics-of-failure as a reliability driver in power electronics,” *IEEE J. Emerg. Sel. Topics Power Electron.*, vol. 2, no. 1, pp. 97–114, Mar. 2014.

[3] B. Ji, V. Pickert, W. Cao, and B. Zahawi, “In situ diagnostics and prognostics of wire bonding faults in IGBT modules for electric vehicle drives,” *IEEE Trans. Power Electron.*, vol. 28, no. 12, pp. 5568–5577, Dec. 2013.

[4] S. Yang, D. Xiang, A. Bryant, P. Mawby, R. Li, and P. Tavner, “Condition monitoring for device reliability in power electronic converters: A review,” *IEEE Trans. Power Electron.*, vol. 25, no. 11, pp. 2734–2752, Nov. 2010.

[5] Y. Song and B. Wang, “Survey on reliability of power electronic systems,” *IEEE Trans. Power Electron.*, vol. 28, no. 1, pp. 591–604, Jan. 2013.

[6] S. Yang, A. Bryant, P. Mawby, D. Xiang, L. Ran, and P. Tavner, “An industry-based survey of reliability in power electronic converters,” *IEEE Trans. Ind. Appl.*, vol. 47, no. 3, pp. 1441–1451, May/Jun. 2011.

[7] M. Ciappa, “Selected failure mechanisms of modern power modules,” *J. Microelectron. Rel.*, vol. 42, nos. 4–5, pp. 653–667, Apr./May, 2002.

[8] Y. Yamada *et al.*, “Reliability of wire-bonding and solder joint for high temperature of power semiconductor device,” *J. Microelectron. Rel.*, vol. 47, no. 12, pp. 2147–2151, Dec. 2007.

[9] V. Smet *et al.*, “Ageing and failure models of IGBT modules in high temperature power cycling,” *IEEE Trans. Ind. Electron.*, vol. 58, no. 10, pp. 4931–4941, Oct. 2011.

[10] H. Huang and P. A. Mawby, “A lifetime estimation technique for voltage source inverters,” *IEEE Trans. Power Electron.*, vol. 28, no. 8, pp. 4113–4119, Aug. 2013.

[11] D. Murdock, J. Torres, J. Connors, and R. Lorenz, “Active thermal control of power electronic modules,” *IEEE Trans. Ind. Appl.*, vol. 42, no. 2, pp. 552–558, Mar./Apr. 2006.

[12] D. Hirschmann, D. Tissen, S. Schroder, and R. W. De Doncker, “Reliability prediction for inverters in hybrid electrical vehicles,” *IEEE Trans. Power Electron.*, vol. 22, no. 6, pp. 2511–2517, Nov. 2007.

[13] C. S. Yun, P. Regli, J. Waldmeyer, and W. Fichtner, “Static and dynamic thermal characteristics of IGBT power modules,” in *Proc. 11th Int. Symp. Power Semicond. Devices ICs*, 1999, pp. 37–40.

[14] C. S. Yun, P. Malberti, M. Ciappa, and W. Fichtner, “Thermal component model for electrothermal analysis of IGBT module systems,” *IEEE Trans. Adv. Packag.*, vol. 24, no. 3, pp. 401–406, Aug. 2001.

[15] M. Musallam and C. M. Johnson, “Real-time compact thermal models for health management of power electronics,” *IEEE Trans. Power Electron.*, vol. 25, no. 6, pp. 1416–1425, Jun. 2010.

[16] B. Du, J. L. Hudgins, E. Santi, A. T. Bryant, P. R. Palmer, and H. A. Mantooth, “Transient electrothermal simulation of power semiconductor devices,” *IEEE Trans. Power Electron.*, vol. 25, no. 1, pp. 237–248, Jan. 2010.

[17] M. Ishiko and T. Kondo, “A simple approach for dynamic junction temperature estimation of IGBTs on PWM operating conditions,” in *Proc. IEEE Power Electron. Spec. Conf.*, Jun. 2007, pp. 916–920.

[18] I. Swan, A. Bryant, P. A. Mawby, T. Ueta, T. Nishijima, and K. Hamada, “A fast loss and temperature simulation method for power converters—Part II: 3-D thermal model of power module,” *IEEE Trans. Power Electron.*, vol. 27, no. 1, pp. 258–268, Jan. 2012.

[19] V. Blasko, R. Lukaszewski, and R. Sladky, “On line thermal model and thermal management strategy of a three phase voltage source inverter,” in *Proc. IEEE Ind. Appl. Soc. Annu. Meeting*, Phoenix, AZ, USA, 1999, pp. 1423–1431.

[20] J. Lemmens, P. Vanassche, and J. Driesen, “Optimal control of traction motor drives under electrothermal constraints,” *IEEE J. Emerg. Sel. Topics Power Electron.*, vol. 2, no. 2, pp. 249–263, Jun. 2014.

[21] J. J. Nelson, G. Venkataramanan, and A. M. El-Refaie, “Fast thermal profiling of power semiconductor devices using Fourier techniques,” *IEEE Trans. Ind. Electron.*, vol. 53, no. 2, pp. 521–529, Apr. 2006.

[22] Z. Luo, H. Ahn, and M. A. E. Nokali, “A thermal model for insulated gate bipolar transistor module,” *IEEE Trans. Power Electron.*, vol. 19, no. 4, pp. 902–907, Jul. 2004.

[23] T. K. Gachovska, B. Tian, J. L. Hudgins, W. Qiao, and J. F. Donlon, “A real-time thermal model for monitoring of power semiconductor devices,” *IEEE Trans. Ind. Appl.*, vol. 51, no. 4, pp. 3361–3367, Jul./Aug. 2015.

[24] A. Bryant *et al.*, “A fast loss and temperature simulation method for power converters—Part I: Electrothermal modeling and validation,” *IEEE Trans. Power Electron.*, vol. 27, no. 1, pp. 248–257, Jan. 2012.

[25] Y. Jiao, S. Lu, and F. C. Lee, “Switching performance optimization of a high power high frequency 3-level active neutral point clamped phase leg building block,” *IEEE Trans. Power Electron.*, vol. 29, no. 7, pp. 3255–3266, Feb. 2014.

[26] Z. Zhou, M. S. Kanniche, S. G. Butcup, and P. Igic, “High-speed electrothermal simulation model of inverter power modules for hybrid vehicles,” *IET Elect. Power Appl.*, vol. 5, no. 8, pp. 636–643, Sep. 2011.

[27] L. Dupont, Y. Avenas, and P. O. Jeannin, “Comparison of junction temperature evaluations in a power IGBT module using an IR camera and three thermosensitive electrical parameters,” *IEEE Trans. Ind. Appl.*, vol. 49, no. 4, pp. 1599–1608, Jul./Aug. 2013.

[28] M. N. Sabry and H. S. Abdelmeguid, “Compact thermal models: A global approach,” *ASME J. Electron. Packag.*, vol. 130, no. 4, pp. 041107-1–041107-6, Dec. 2008.

[29] M. Musallam, C. M. Johnson, and C. Buttay, “Real-time compact electronic thermal modeling for health monitoring,” in *Proc. 12th Eur. Conf. Power Electron. Appl.*, Sep. 2007, pp. 1–10.

[30] V. Szekely and M. Rencz, “Increasing the accuracy of thermal transient measurements,” *IEEE Trans. Compon. Packag. Technol.*, vol. 25, no. 4, pp. 539–546, Dec. 2002.

[31] M. Rencz and V. Székely, “Non-linearity issues in the dynamic compact model generation,” in *Proc. IEEE 19th Annu. Semicond. Therm. Meas. Manag. Symp.*, San Jose, CA, USA, Mar. 2003, pp. 263–270.

[32] M. Rencz and V. Székely, “Studies on the nonlinearity effects in dynamic compact model generation of packages,” *IEEE Trans. Compon. Packag. Technol.*, vol. 27, no. 1, pp. 124–130, Mar. 2004.

Jin Ye (S’13–M’14) received the B.S. and M.S. degrees in electrical engineering from Xi’an Jiaotong University, Xi’an, China, in 2008 and 2011, respectively, and the Ph.D. degree in electrical engineering from McMaster University, Hamilton, ON, Canada, in 2014.

She was a Postdoctoral Research Associate at the McMaster Institute for Automotive Research and Technology, McMaster University, Hamilton. She is currently an Assistant Professor of electrical engineering with San Francisco State University, San Francisco, CA, USA. Her main research interests include power electronics, electric motor drives, renewable energy conversion, and electrified transportation.

Kai Yang received the B.S. degree in thermal energy and power engineering from the Beijing University of Aeronautics and Astronautics, Beijing, China, in 2009 and the M.S. degree in mechanical engineering from McMaster University, Hamilton, ON, Canada, in 2014.

He is currently a Product Designer at Bombardier Transportation Inc., Kingston, ON, Canada, focusing on the mechanical and electrical design and thermal analysis of trains and its subsystems. His research interests include the thermal management system design of traction inverters and power electronic devices. He was the recipient of National Scholarship in China and started his own company as the Chief Mechanical Engineer in China from 2010 to 2012.

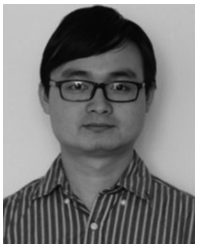

Haizhong Ye received the B.S. and M.S. degrees in electrical engineering from Xi’an Jiaotong University, Xi’an, China, in 2007 and 2010, respectively, and the Ph.D. degree in electrical engineering from the McMaster Institute for Automotive Research and Technology, McMaster University, Hamilton, ON, Canada, in 2014.

He is currently a Power Electronics Design Engineer at Schneider Electric Solar Business, Burnaby, BC, Canada. His main research interests include automotive power electronics, renewable energy conversion, and high power applications.

Ali Emadi (S’98–M’00–SM’03–F’13) received the B.S. and M.S. degrees in electrical engineering with highest distinction from the Sharif University of Technology, Tehran, Iran, in 1995 and 1997, respectively, and the Ph.D. degree in electrical engineering from Texas A&M University, College Station, TX, USA, in 2000.

He is the Canada Excellence Research Chair in Hybrid Powertrain at McMaster University, Hamilton, ON, Canada. Before joining McMaster University, he was the Harris Perlstein Endowed Chair Professor of Engineering and the Director of the Electric Power and Power Electronics Center and Grainger Laboratories at Illinois Institute of Technology (IIT) in Chicago, IL, USA, where he established research and teaching facilities as well as courses in power electronics, motor drives, and vehicular power systems. He was the Founder, the Chairman, and the President of Hybrid Electric Vehicle Technologies, Inc.,—a university spin-off company of IIT. He is the principal author/coauthor of more than 350 journal and conference papers as well as several books including *Vehicular Electric Power Systems* (2003), *Energy Efficient Electric Motors* (2004), *Uninterruptible Power Supplies and Active Filters* (2004), *Modern Electric, Hybrid Electric, and Fuel Cell Vehicles* (2nd ed, 2009), and *Integrated Power Electronic Converters and Digital Control* (2009). He is also the Editor of the *Handbook of Automotive Power Electronics and Motor Drives* (2005), and *Advanced Electric Drive Vehicles* (2014).

Dr. Emadi received numerous awards and recognitions. He was the Advisor for the Formula Hybrid Teams at IIT and McMaster University, which received the GM Best Engineered Hybrid System Award at the 2010, 2013, and 2015 competitions. He was the Inaugural General Chair of the 2012 IEEE Transportation Electrification Conference and Expo and has chaired several IEEE and SAE conferences in the areas of vehicle power and propulsion. He is the founding Editor-in- Chief of the IEEE TRANSACTIONS ON TRANSPORTATION ELECTRIFICATION.